Contents lists available at ScienceDirect

Applied Catalysis B: Environmental

In-situ synthesis of single-atom CoN$_x$ clusters-decorated TiO$_2$ for highly efficient charge separation and CO$_2$ photoreduction

Peng Zeng [a,*,1], Haoran Liu [b,1], Huaiyang Jia [b], Jiayi Cai [a], Xueer Deng [a], Tianyou Peng [b,*,2]

[a] *School of Food and Pharmaceutical Engineering, Zhaoqing University, Zhaoqing 526061, China*
[b] *College of Chemistry and Molecular Sciences, Wuhan University, Wuhan 430072, China*

ARTICLE INFO

ABSTRACT

Solar-driven CO$_2$ reduction reaction (CO$_2$RR) to produce chemical fuels is an attractive way to alleviate the greenhouse effect and energy crisis. Herein, a novel single-atom CoN$_x$ clusters-decorated TiO$_2$ (CoN$_x$/TiO$_2$) is synthesized *in situ* by calcining a composite derived from immersing a metal organic framework (Mil-125) into cobalt *tetra*(4-pyridyl)porphyrin (CoPy$_4$) solution. The resultant CoN$_x$/TiO$_2$ delivers an excellent CO$_2$RR activity with CO/CH$_4$ yields of 24.4/119.9 μmol g^{-1} h^{-1}, corresponding an overall photoactivity of 1007.6 μmol g^{-1} h^{-1}, 10.6 time higher than that of TiO$_2$ alone. It is found that CoPy$_4$ molecules can enter Mil-125′s micropores, which helps to pyrolyze CoPy$_4$ into highly dispersed single-atom-contained CoN$_x$ clusters and to form strong interaction with the primary nanoparticles of TiO$_2$ *quasi*-nanocube-like aggregated particles derived from Mil-125. These factors of CoN$_x$/TiO$_2$ enable efficient photogenerated charge separation, strong chemical adsorption to reactants and high atom utilization, thus providing a new strategy for constructing TiO$_2$-based photocatalysts with highly dispersed single-atom catalytic sites for CO$_2$ photoreduction.

1. Introduction

Converting CO$_2$ into chemical fuels not only can alleviate the problems of fossil resources' rapid depletion and growing CO$_2$ emissions, but also can help to achieve the carbon balance of the Earth [1–3]. Among which, solar-driven CO$_2$ reduction reaction (CO$_2$RR) has been recognized as a potential artificial photosynthesis technology, thus seeking efficient photocatalysts that can achieve CO$_2$ photoreduction has become a hot topic [4]. Among various photocatalysts developed, TiO$_2$ is the most studied one due to its low-cost, non-toxic, excellent physicochemical stability and UV light-driven photoactivity [5,6]. However, the photocatalytic system with single TiO$_2$ still faces severe photogenerated charge recombination, narrow spectral absorption and low quantum efficiency [4]. Therefore, various strategies have been adopted to improve the charge separation, spectral absorption and photoactivity of TiO$_2$-based materials [7–10]. Among them, loading of cocatalyst is recognized as one of the simplest and most effective methods [4,11–13].

Although precious metals such as Pt, Pd and Au are widely used as cocatalysts due to their low activation energy and effective charge separation, the high costs limit their large-scale applications [11,12],

and thus certain transition metals such as Fe, Co, Ni and Cu have been developed as cocatalysts [4,13]. Another promising approach is to develop single-atom catalysts with evenly distributed and coordinatively unsaturated sites, which have advantages such as unique electronic structure, high atom utilization, effective adsorption/activation of reactants and strong catalytic activity [14–23]. For instance, a Cu single-atom site-containing Au-Cu alloy nanoparticles-decorated TiO$_2$ was prepared *via* a photodeposition method, which delivers a record-high CO$_2$RR photoactivity with a CH$_4$ yield up to 3578.9 μmol g^{-1} h^{-1} and a CH$_4$ selectivity of 77.1% [23]. It proved that the synergistic function of Cu single-atoms and Au-Cu alloy nanoparticles enhance the adsorption activation of reactants and lower the overall activation energy barrier for the CH$_4$ production, thus contributing to an effective cocatalyst for photocatalytic CO$_2$RR [23].

Recently, atomically dispersed M-N$_x$ clusters in the samples have been identified as the active sites for catalyzing various reactions such as CO$_2$ and O$_2$ reductions as well as H$_2$S oxidation [24–28]. For instance, a hollow fiber stitched by carbon nanotube with enriched M-N$_4$ single-atom sites achieves fast kinetics, high activity and good durability on catalyzing CO$_2$RR [24]. Density functional theory calculations also

---

demonstrate that the local coordination environment of single-atoms supported on conjugated N_4-macrocyclic ligands (Co-N_4-CPY) and its analogues (where one of the N atoms substituted by O (Co-N_3O-CPY) or C (Co-N_3C-CPY)) can disrupt the symmetry of primary Co-N_4 ligand field and induce charge redistribution of the Co center, which then influence the energy barrier of CO_2 to *COOH and the desorption process of *CO, thus resulting in different CO_2RR pathways [21]. In general, it is difficult to preferentially build local electronic structures around M-N_x site and improve its catalytic activity [24,25], and therefore it is necessary to explore effective strategy to construct M-N_x photocatalysts with both optimized external architecture and internal local coordination environment to jointly improve the CO_2RR activity.

Metal porphyrins and their analogues have clear M-N_4 coordination structures and well-defined single-atom active sites, which can be systematically tuned to achieve high activity and product selectivity. Therefore, a series of metalporphyrins and their heterometallic conjugated polymers were synthesized in our group, and it was found that the highly dispersed M-N_4 subunits can serve as single-atom catalytic sites to greatly enhance the photo(electro)catalytic CO_2RR or H_2 production performance [17–19,29–32]. By considering that the well-defined and coordinatively unsaturated M-N_4 subunits of metalloporphyrins can also act as the precursor of highly dispersed M-N_x single-atom active sites, we introduce an *in-situ* synthesis procedure of CoN_x clusters-modified TiO_2 (CoN_x/TiO_2) as shown in Scheme 1, whereby the cobalt *tetra*(4-pyridyl) porphyrin (CoPy$_4$) was synthesized *via* a two-step procedure according to our previous method [30–32], and the Ti-based metal organic framework (MOF) Mil-125 constructed from Ti-O clusters and terephthalic acid (H$_2$BDC) was prepared according to the literatures [33–35]. The Mil-125 was immersed into the CoPy$_4$ N,N-dimethylformamide (DMF) solution to give CoPy$_4$/Mil-125 composite, which was calcined to *in-situ* form CoN_x/TiO_2. During the calcination process, the CoPy$_4$ molecules containing Co-N_4 subunits can be pyrolyzed into CoN_x clusters, which serve as the single-atom active sites of photocatalytic CO_2RR and ~~to~~ form strong interaction with the primary nanoparticles of TiO_2 *quasi*-nanocube-like aggregated particles formed by the calcination of Mil-125. The effects of CoN_x clusters on the microstructure, spectral absorption, energy band structure, adsorption and activation of reactants (CO_2/H_2O) and photogenerated charge separation of TiO_2 were systematically studied, and the enhancement mechanism of the photocatalytic CO_2RR activity of CoN_x/TiO_2 was deeply discussed.

2. Experimental

2.1. Material preparation

Mil-125 precursor was prepared according to the literatures (Scheme 1) [33–35]. Typically, 6.0 g of terephthalic acid (H$_2$BDC) was dissolved in 54 mL of DMF under stirring, then 12 mL of methanol and 2.4 mL of tetrabutyl titanate (lower than the stoichiometric ratio of 20 wt% to form Ti defects in the MOF) were added. After stirring for 10 min, the resulting solution was transferred into PTFE-lined autoclave (volume of 200 mL), then hydrothermally treated at 130 °C for 20 h. After that, the precipitate was separated by centrifugation, washed three times with DMF and methanol in successive, then vacuum dried at 70 °C for 6 h to give the Mil-125 precursor. The X-ray diffraction (XRD) pattern, liquid N_2 adsorption/desorption experiments and elemental analysis results prove the successful synthesis of Mil-125 containing two kinds of accessible micropores with pore sizes of 12.55 and 6.13 Å (Scheme 1, Fig. S1 and Table S1 as well as the corresponding analyses) [33–35].

CoPy$_4$ precursor was synthesized *via* a two-step procedure according to our previous method with slight modification (Scheme 1) [30–32]. Typically, 4-pyridine formaldehyde (5.60 g, 50 mmol) was dissolved in 200 mL of propionic acid (PA), then refluxed at 140 °C for 30 min. After that, a newly evaporated pyrrole (3.36 mg, 50 mmol) was mixed with 10 mL of PA to obtain a pyrrole solution, which was added dropwise to the above solution. The mixture was refluxed in N_2 atmosphere at 140 ℃ for 8 h. After cooling, the PA was removed by vacuum distillation, and the black solid was added into 30 mL of DMF overnight. The precipitate was separated by filtration, washed with ether for three times to give crude sample, which was purified by silica gel column chromatography with dichloromethane/methanol (15:1, v/v) solvent, then recrystallized in dichloromethane/n-hexane solvent to give the *tetra*(4-pyridyl)porphyrin (H$_2$Py$_4$). The H$_2$Py$_4$ (100 mg, 0.16 mmol) and Co(OAc)$_2$·4 H$_2$O (174.4 mg, 0.70 mmol) were dispersed in 30 mL of DMF, then refluxed at 150 ℃ for 12 h. After that, the precipitate was separated through centrifugation, washed several times with deionized water, and vacuum dried overnight at 70 ℃ to give the CoPy$_4$. Yield 98.8 mg, 91.0%. TOF-MS (*m/z*): 675.5, C$_{40}$H$_{24}$N$_8$Co ([M+H]$^+$ = 675.6).
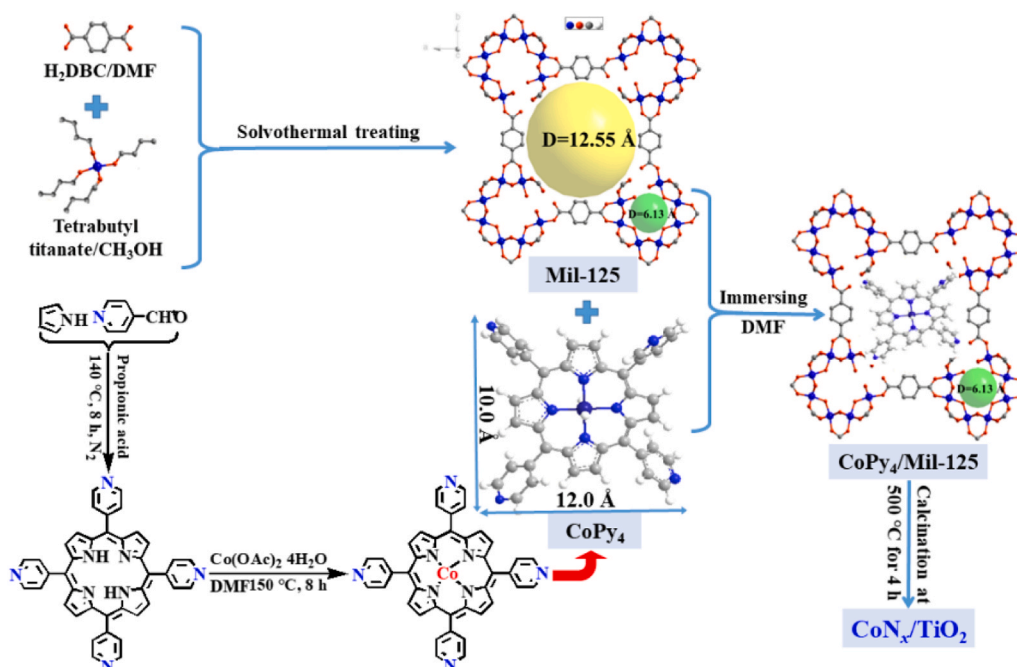
Scheme 1. Schematic diagram of *in-situ* synthesis route of the CoN_x/TiO_2.

EA ($C_{40}H_{24}N_8Co$): Calcd. C 71.11, H 3.58, N 16.59; Found C 71.36, H 3.73, N 16.35. UV–vis (λ_{max}(DMF)/nm): 413, 537.

CoN_4/TiO_2 was synthesized *via* a two-step procedure (Scheme 1). Typically, 500 mg of Mil-125 was added into 40 mL of $CoPy_4$ (4.0 mg) DMF solution. After stirring for 5 h, the DMF was removed by rotary evaporation, the solid was washed three times with deionized water, and vacuum dried at 100 °C to give the $CoPy_4$/Mil-125 composite, which was placed in a muffle furnace for calcination at 500 °C for 4 h with a heating rate of 5 °C min^{-1} to give the CoN_x/TiO_2. By varying $CoPy_4$ addition amount, a series of CoN_x/TiO_2 products were obtained. For comparison, CoO_x/TiO_2 was prepared as follows: 500 mg of Mil-125 was added into 40 mL of deionized water containing 0.8 mg of anhydrous $CoCl_2$ (Co weight percentage in $CoCl_2$/Mil-125 is equivalent to that of $CoPy_4$/Mil-125). After stirring for 5 h, the water was removed by rotary evaporation, the solid was washed three times with deionized water, and vacuum dried at 100 °C to give the $CoCl_2$/Mil-125 composite, which was placed in a muffle furnace for calcination at 500 °C for 4 h with a heating rate of 5 °C min^{-1} to give the CoO_x/TiO_2.

2.2. Material characterization

The X-ray diffraction (XRD) patterns of samples were acquired on a Miniflex 600 X-ray diffractometer with CuKα source ($\lambda = 0.154$ nm) operated at 40 kV, 20 mA and scanning rate of 10 ° min^{-1}. Fourier transform infrared spectroscopy (FTIR) was conducted on a Biorad FTS-165 FT-IR spectrometer using KBr pellet. Verios Field Emission Scanning Electron Microscopy (FESEM) was used to observe the morphology of samples, and High-Resolution Transmission Electron Microscopy (HRTEM) was obtained on LaB6 JEM-2100(HR) electron microscope (JEOL Ltd.) with a working voltage of 200 kV. JEOL JEM-ARM200F Aberration Correction High Angle Annular Dark Field Scanning Transmission Electron Microscope (AC-HAADF-STEM) equipped with an energy dispersive X-ray (EDX) spectrometer was used to observe the microstructures performed at 200 kV using microscope and Schottky cold field gun. Liquid N_2 adsorption /desorption experiments were conducted at 77 K on a Micrometrics ASAP 2460 system. Except for Mil-125, other samples were degassed at 200 °C for 6 h before test.

Element contents in samples were analyzed using an EA3000 element analyzer, and the metal contents were determined using a JXA-8530 F Plus Field Emission Electron Probe Analyzer (EPMA) or an IRIS Intrepid II XSP Inductively Coupled Plasma-Atomic Emission Spectrometer (ICP-AES). UV-Vis absorption spectrum was measured on a TU-1810 spectrophotometer. UV-Vis diffuse reflectance absorption spectra (DRS) were measured on an Agilent Cary 5000 spectrophotometer equipped with an integrating sphere with $BaSO_4$ as a reference. Photoluminescence (PL) spectra were acquired on a Hitachi F-4600 fluorescence spectrophotometer under excitation wavelength (λ_{ex}) of 375 nm. Time resolved fluorescence decay spectra (TRFS) was obtained on an Edinburgh FES 920 femtosecond fluorescence spectrophotometer under λ_{ex} of 375 nm, emission wavelength (λ_{em}) of 460 nm. Element valence states and valence band (VB) spectra were measured on a Thermo Fisher ESCALAB 250Xi X-ray photoelectron spectrometer (XPS) equipped with a monochromatic source (AlKα) operated at 300 W and calibrated with contaminated C 1 *s* at 284.8 eV.

Photocurrent time curves (*i-t*) and electrochemical impedance spectroscopy (EIS) were measured in a traditional three-electrode system using 0.5 M Na_2SO_4 solution as electrolyte with Pt foil and Ag/AgCl electrode as counter electrode and reference electrode, respectively. The working electrode was prepared by dropping the Nafion solution containing the sample onto a pre-cleaned FTO glass (1.0 × 1.0 cm²). If necessary, a 300 W Xe-lamp was used as light source to illuminate the working electrode. Before the electrochemical testing, the three-electrode system was blown with N_2 flow for 0.5 h.

Temperature programmed desorption-mass spectrometry (TPD-MS) for CO_2/H_2O on the samples were conducted on an AutoChem1 II 2920 temperature programmed chemical adsorption analyzer equipped with a Hiden QIC-20 mass spectrometer. Typically, 0.10 g of sample was placed in a sample cell, degassed at 120 °C for 8 h in an Ar flow, and then slowly cooled to 80 °C. A 10% CO_2/Ar mixed gas containing water vapor was introduced to adsorb CO_2/H_2O fully. After 2 h, the sample was purged with an Ar flow for 30 min to remove CO_2/H_2O that had not been adsorbed. Each sample was heated to 800 °C in Ar at a rate of 10 °C min^{-1}, while the CO_2 ($m/z = 44$) and H_2O ($m/z = 18$) mass signals were recorded by mass spectrometry.

Co *K*-edge X-ray absorption spectra (XAS) were measured *via* a transmission mode of BL11B beamline of Shanghai Synchrotron Radiation Facility (SSRF) with the storage ring's beam current of 220 mA in a top-up mode, the incident photons monochromatized by Si(111) double-crystal monochromator with an energy resolution ($\Delta E/E = \sim 1.4 \times 10^{-4}$). The energy was calibrated using Cu foil (8979 eV), and the rejection of higher harmonics was achieved by a pair of Rh-coated mirrors at 4 mrad. The incident beam intensity (I_0) was detected with the ion chamber filled with Ar gas, and Ar gas was adopted to detect the transmitted beam intensity (I_t). The spot size of sample was 200 × 250 μm (H × V). The raw data were analyzed by IFEFFIT software package after calibrated, averaged, pre-edge background subtracted and post-edge normalized through Athena program [36]. Fourier transformation of the k^3-weighted extended X-ray absorption fine structure (EXAFS) oscillations ($k^3\chi(k)$) from *K*-space to *R*-space was done in a range of 3.0–10.0 Å^{-1} to obtain the radial distribution function, and the data were fitted using Artemis program [37]. In addition, wavelet transform contour plots were obtained based on Morlet wavelets ($\kappa = 10$, $\sigma = 1$) by processing *k*-space data with HamaFortran and SigmaPlot softwares [38].

2.3. Photocatalytic CO_2RR performance measurement

Photocatalytic CO_2RR experiments were performed in a gas-closed reactor (Pyrex glass) with a volume of 500 mL under 300 W Xe-lamp illumination. Typically, photocatalyst (10 mg) was dispersed in ethanol, and then dropped on a quartz plate in a watch glass under infrared lamp. After the ethanol was evaporated, the watch glass was placed in the reactor, then $NaHCO_3$ (1.65 g) was added into the bottom of reactor, which was then sealed, and completely removed the air using vacuum pump. After repeating the above degassing operation three times, 5.0 mL of H_2SO_4 solution (4.0 M) was introduced into the reactor to generate CO_2/H_2O vapor. During the illumination, 2 mL of gas was extracted using a syringe at each interval of 1.0 h, and the gas concentration was analyzed using a SP7820 gas chromatograph (TDX-01 column, Rainbow Co. Ltd.) equipped with a flame ionized detector (FID) and methanator. Moreover, a Shimadzu GC-2010 gas chromatography equipped a BID detector was used to detect the possible other reduced products such as H_2, O_2, C_2H_4, C_2H_6 and CH_3OH in the photoreaction system, and a Bruker Ascend 400 ^{1}H NMR spectrophotometer was used to detect the possible reduced products such as HCOOH, CH_3OH or HCHO in the acetic ether extract of the solution in the reactor bottom.

The main reduced products in the present photocatalytic CO_2RR system are only CH_4 and CO, and no other reduced product such as C_2H_4, CH_3OH, C_2H_5OH (using GC-FID or GC-BID detector) or HCOOH, HCHO, CH_3OH (using ^{1}H NMR spectrum) were detected. The produced amounts of CH_4/CO gases in the reactor were calibrated with a standard CH_4/CO gas mixture. Due to the different number of electrons required for the CO and CH_4 production, total consumed electron number (TCEN) was used to evaluate the overall photoactivity for CO_2RR using Eq. (1) [4,32].

$$TCEN = \frac{(2 \times c_{CO} + 8 \times c_{CH_4}) \times V_{rea.}}{m_{cat.} \times t_{irr.}} \tag{1}$$

where c_{CO} and c_{CH_4} are the produced CO and CH_4 concentrations in the photoreactor, respectively. $V_{rea.}$ is the reactor volume. $m_{cat.}$ is the photocatalyst dosage, and $t_{irr.}$ is the irradiation time.

3. Results and discussion

3.1. Crystal and microstructure analyses

The XRD patterns (Fig. 1a) indicate that the calcined product of Mil-125 is a mixed crystal phase of TiO_2, mainly composed of anatase (JCPDS No. 21–1272) with a small amount of rutile (JCPDS No. 21–1276) [33]. However, the calcined product (CoN_x/TiO_2) of $CoPy_4$/Mil-125 composite displays a pure anatase, implying that the introduced $CoPy_4$ molecules can affect the pyrolysis of Mil-125, and then the crystal phase of the calcined product (TiO_2). Similarly, the calcined product (CoO_x/TiO_2) of $CoCl_2$/Mil-125 does not show obvious rutile phase, indicating that cobalt salt also affects the pyrolysis of Mil-125 and the crystal phase of TiO_2. Moreover, CoN_x/TiO_2 and CoO_x/TiO_2 show no any characteristic diffraction peak of metal oxides other than TiO_2. When the addition amount per 500 mg of Mil-125 is increased by five-fold ($CoPy_4$ (20 mg) and $CoCl_2$ (4.0 mg)), the relative calcined products (CoN_x/TiO_2-20 and CoO_x/TiO_2-4.0) display the characteristic (311), (220), (440) and (511) diffraction peaks of Co_3O_4 (JCPDS No. 42–1467) (Fig. 1b), indicating that the excessive $CoPy_4$ or $CoCl_2$ coated on the Mil-125 particles without entering the MOF's micropores would be likely to form cobalt oxide after the calcination process.

FESEM and TEM images indicate that Mil-125 exhibits a *quasi*-nanocube-like morphology with uneven particle sizes of *ca.* 200–300 nm (Fig. 2a,b), which is similar to the literature [34,35], while its calcined product (TiO_2) has similar *quasi*-nanocube-like structure with uneven particle size distribution (Fig. 2c,d). Different from the Mil-125 (Fig. S2a), the *quasi*-nanocube-like structure of TiO_2 is stacked by ultrafine irregular primary nanoparticles (Fig. S2b), implying the Mil-125 was transformed into ultrafine TiO_2 nanoparticles, which aggregate into *quasi*-nanocube-like aggregated particless with particle sizes of *ca.* 300–600 nm. $CoPy_4$/Mil-125 composite still retains the original morphology of Mil-125 with smooth surface (Fig. 2e,f), and its calcined product (CoN_x/TiO_2) displays similar *quasi*-cube-like aggregated particless with a particle sizes of *ca.* 300–500 nm (Fig. 2g,h), and the HRTEM images (Fig. S2c,d) indicate that both $CoPy_4$/Mil-125 and CoN_x/TiO_2 still have smooth surface, while the CoN_x/TiO_2 is composed of stacked ultrafine primary nanoparticles like the TiO_2.

Differently, $CoCl_2$/Mil-125 composite shows a significant changed surface morphology with a large number of small nanoparticles attached on its *quasi*-nanocube surfaces (Fig. 2i,j), and its calcined product (CoO_x/TiO_2) show that the *quasi*-nanocube surfaces with diameter of *ca.* 300–500 nm were attached by aggregation of ultrafine primary nanoparticles (Fig. 2k,l), which can be confirmed by the HRTEM images of $CoCl_2$/Mil-125 and CoO_x/TiO_2 (Fig. S2e,f). It implies that during the loading of $CoCl_2$, its hydrolysates cannot (or cannot fully) enter the Mil-125's micropores, but rather adhere a large amount on the particle surfaces, which were converted into CoO_x ultrafine nanoparticles after the calcination, and thus presenting a morphology different from TiO_2 and CoN_x/TiO_2. These results indicate that $CoPy_4$ molecules can enter Mil-125's micropores through the accessible pores (12.55 Å, Scheme 1), while the hydrolysates of $CoCl_2$ are adhered on the Mil-125 particle surfaces. This difference may affect the thermal decomposition behavior of Mil-125-based composite, and then the microstructure and composition of the calcined product.

TEM and HRTEM images of CoN_x/TiO_2 show that the single *quasi*-nanocube has the lattice stripe spacing of ~0.352 nm of anatase (101) facets (Fig. 3a,b), and the high angle annular dark field scanning transmission electron microscope (AC-HADDF-STEM) image indicates some bright contrast spots of Co atoms in TiO_2 lattice (Fig. 3c). The line scanning profiles alone the randomly selected yellow lines (Fig. 3d) shows that Line 1 contains three Co atoms and Line 2 contains two Co atoms. It should be noted that no lattice stripe spacing related to the cobalt oxides was observed in the HRTEM image of CoN_x/TiO_2 (Fig. 3b), which may be due to the high distribution of CoN_x clusters in the TiO_2 matrix.

AC-HADDF-STEM image and its corresponding energy dispersive X-ray (EDX) element mappings (Fig. 3e) show uniform distributions of Ti, O, Co and N elements in the single *quasi*-nanocube of CoN_x/TiO_2, implying that $CoPy_4$ molecules can more effectively enter Mil-125's micropores than $CoCl_2$, and then pyrolyzed to form CoN_x clusters during the calcination. The locally amplified AC-HAADF-STEM image and its corresponding EDX element mappings (Fig. 3f) can further demonstrate this conjecture. As seen, Ti and O elements are abundant and evenly distributed, while Co and N elements have very low contents and highly dispersity. Moreover, the overlay pattern of Co/N elements (Fig. S3) clearly shows that the main distribution areas of Co and N are very close, implying the formation of CoN_x clusters on the ultrafine primary nanoparticles of the TiO_2 aggregated *quasi*-nanocube with close contact after the calcination.

Elemental analysis results (Table 1) show that the CoN_x/TiO_2 contains a small amount of N elements, implying that some N elements of $CoPy_4$ are retained in the calcined product, which may modify the TiO_2 surface and serve as anchoring sites for Co atoms, and the N/Co molar ratio (3.88) is slightly lower than 4.0, further proving the formation of CoN_x clusters in CoN_x/TiO_2. The FTIR spectrum of CoN_x/TiO_2 show no any characteristic IR bands of $CoPy_4$, demonstrating the macrocyclic structure of $CoPy_4$ molecule is completely destroyed (Fig. S4a and the corresponding analyses) [26]. Thermogravimetric analyses (TGA) results indicate that the weight losses of TiO_2, CoN_x/TiO_2 and CoO_x/TiO_2 can be basically ignored in the range of 30–650 °C (Fig. S4b,c and the corresponding analyses), which is consistent with the EA results
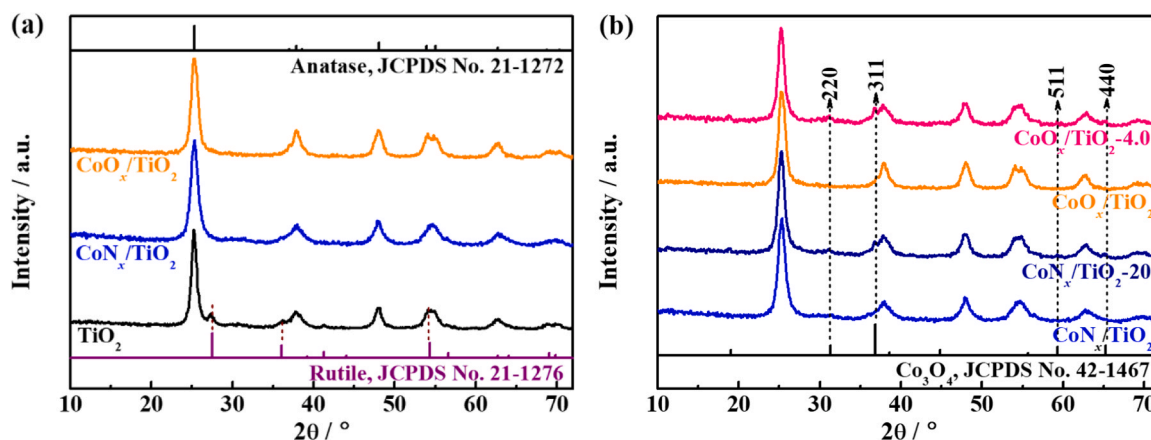

Fig. 1. (a) XRD patterns of the TiO_2, CoN_x/TiO_2 and CoO_x/TiO_2 derived from the Mil-125 and its composites. (b) Comparison of XRD patterns of the CoN_x/TiO_2 and CoO_x/TiO_2 derived from the Mil-125-based composites with different $CoPy_4$ (4.0, 20 mg) and $CoCl_2$ (0.8, 4.0 mg) addition amounts.
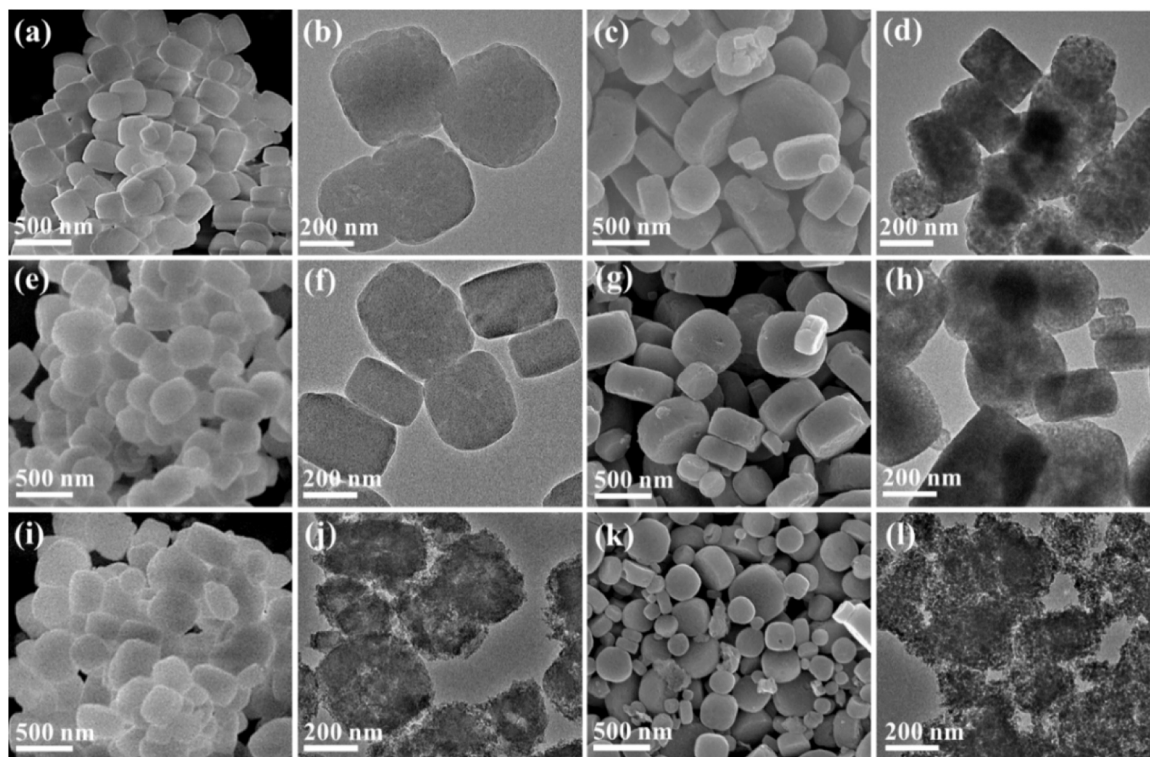
Fig. 2. FESEM and TEM images of the Mil-125 (a,b) and TiO$_2$ (c,d), CoPy$_4$/Mil-125 (e,f) and CoN$_x$/TiO$_2$ (g,h), CoCl$_2$/Mil-125 (i,j) and CoO$_x$/TiO$_2$ (k,l).
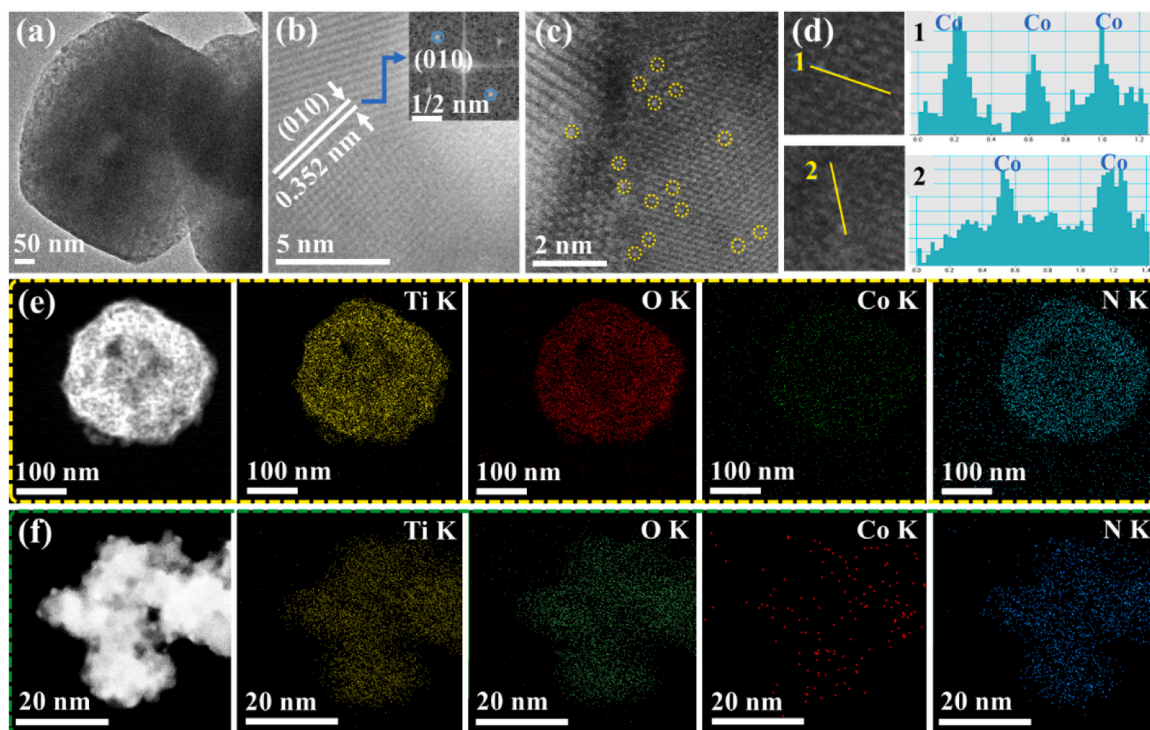

Fig. 3. (a-d) HRTEM images (a,b) and corresponding FFT pattern (inset in b), AC-HADDF-STEM image (c) and corresponding filtered images as well as line scan profiles (d) of the CoN$_x$/TiO$_2$. (e,f) AC-HADDF-STEM images and the Ti, O, Co and N mappings of the CoN$_x$/TiO$_2$ with low (e) and high (f) magnification.

(Table 1). Moreover, the X-ray photoelectron spectrosopic (XPS) results show the N/Co molar ratios of the CoN$_x$/TiO$_2$ before and after Ar$^+$-beam etching at 20 nm remain basically unchanged (Fig. S4d), implying that the coordination environments of Co centers in CoN$_x$/TiO$_2$ are relatively stable and uniform.

Based on the above characterization results, it can be concluded that the CoPy$_4$ molecules can more easily enter the Mil-125's micropores than the hydrolysates of CoCl$_2$, which can influence the pyrolysis behavior of Mil-125, thereby the microstructure and particle size distribution of the product (CoN$_x$/TiO$_2$) derived from CoPy$_4$/Mil-125

Table 1
Elemental analysis results of the TiO$_2$, CoN$_x$/TiO$_2$ and CoO$_x$/TiO$_2$.

Sample	Ti (%)	O (%)	N (%)	C (%)	Co (%)	O/Ti molar ratio	N/Co molar ratio
TiO$_2$	59.83	40.11	–	–	–	2.00	–
CoN$_x$/ TiO$_2$	58.71	40.53	0.35	–	0.38	2.07	3.88
CoO$_x$/ TiO$_2$	58.62	40.67	–	–	0.43	2.09	–

composite are significantly different from the TiO$_2$ and CoO$_x$/TiO$_2$ derived from the single MOF and CoCl$_2$/Mil-125 composite, respectively. This conjecture can be further validated by the liquid N$_2$ adsorption/desorption experiments (Fig. S5 and the corresponding analyses). Compared to the Mil-125 with Type I isotherms, high specific surface area (S_{BET}) and total pore volume (V_{Pore}) (Fig. S1b), those calcined products (TiO$_2$, CoN$_x$/TiO$_2$ and CoO$_x$/TiO$_2$) display significant different liquid N$_2$ adsorption/desorption behaviors with sharply decreased S_{BET}, larger average pore diameter (d_{Pore}) and smaller V_{Pore} (Fig. S5), indicating that the microporous structures of Mil-125 and its composites were collapsed after the calcination. Although the CoN$_x$/ TiO$_2$ retains type IV isotherms similar to the TiO$_2$, it presents much larger S_{BET} (75.8 m^2 g^{-1}) and V_{Pore} (0.20 cm^3 g^{-1}) even though there is a slightly smaller d_{Pore} (8.1 nm) than the TiO$_2$ with S_{BET} of 30.6 m^2 g^{-1}, d_{Pore} of ~10.3 nm and V_{Pore} of ~0.12 cm^3 g^{-1}. It indicates that CoPy$_4$ molecules entering the micropores of Mil-125 can stabilize its MOF structure to some extent, which leads to the significant differences in the pyrolysis behavior of Mil-125 and the microstructure of the corresponding calcined product. Nevertheless, the CoO$_x$/TiO$_2$ displays much larger S_{BET} (92.4 m^2 g^{-1}), d_{Pore} (~15.0 nm) and V_{Pore} (~0.43 cm^3 g^{-1})

than the CoN$_x$/TiO$_2$. As mentioned above, the vast majority of hydrolysates of CoCl$_2$ adhere on the Mil-125 particle surface (Fig. 2i,j), which then results in the formation of ultrafine nanoparticles loaded on the TiO$_2$ aggregated particles derived from the CoCl$_2$/Mil-125 composite (Fig. 2k,l). At the same time, the TiO$_2$ aggregated particles in the CoO$_x$/ TiO$_2$ are more uneven and contain a large number of broken nanoparticles (Fig. 2k,l) than the CoN$_x$/TiO$_2$ (Fig. 2g,h), which can be confirmed by the fact that the Barrett-Joyner-Halenda (BJH) pore size distribution curve of the CoO$_x$/TiO$_2$ is significantly different from that of the CoN$_x$/TiO$_2$ (Fig. S5b). Namely, the mesoporous structure of the CoO$_x$/TiO$_2$ is relatively more disordered, thus resulting in the larger S_{BET}, wider BJH pore distribution and V_{Pore} than the CoN$_x$/TiO$_2$. Moreover, CoPy$_4$ molecules entering Mil-125's micropores undergo pyrolysis to form CoN$_x$ clusters under the localized reducing atmosphere due to the decomposition of organic linkers in Mil-125, which are uniformly dispersed on the ultrafine primary TiO$_2$ nanoparticles through strong interaction. These factors will affect the specific surface area, pore structure, adsorption and activation of reactants on CoN$_x$/TiO$_2$, and ultimately affecting the CO$_2$RR activity as confirmed below.

3.2. Valence state and local coordination environment analyses

The survey XPS spectra (Fig. S6) show that the TiO$_2$, CoN$_x$/TiO$_2$ and CoO$_x$/TiO$_2$ contain Ti, O and C elements, and no N and Co element signals can be observed from the CoN$_x$/TiO$_2$. However, obvious N and Co signals are observed from their high-resolution XPS spectra, further confirming that part of N elements of Co-N$_4$ subunits in CoPy$_4$ molecules can be retained as CoN$_x$ clusters after the calcination. The high-resolution Ti 2p spectra (Fig. 4a) exhibit that the TiO$_2$ shows two binding energy (BE) peaks at 458.78 and 464.52 eV, ascribable to the 2$p_{3/2}$ and 2$p_{1/2}$ of Ti^{4+} species [11], respectively. The O 1s XPS spectra
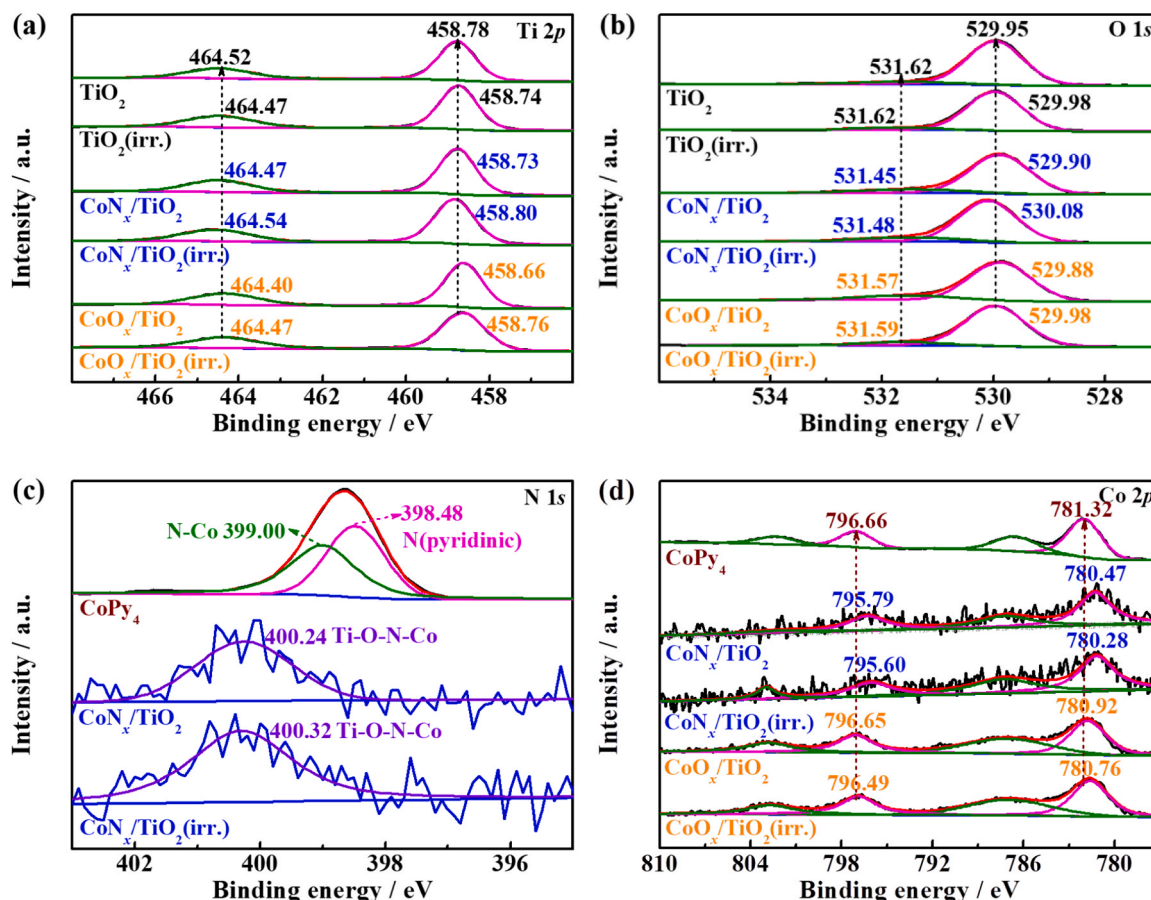

Fig. 4. High-resolution Ti 2p (a), O 1s (b), N 1s (c), Co 2p (d) XPS spectra of the TiO$_2$, CoN$_x$/TiO$_2$ and CoO$_x$/TiO$_2$ before and after 15 min light illumination.

of TiO$_2$ (Fig. 4b) can be deconvoluted into two BE peaks at 529.95 and 531.62 eV, corresponding the O species of lattice and surface hydroxyl of TiO$_2$ [32], respectively. In contrast, the BE peak positions of Ti 2p and O 1s (lattice and surface hydroxyl) of CoN$_x$/TiO$_2$ show a decreasing trend, where the BE values of Ti^{4+} 2p$_{3/2}$/2p$_{1/2}$ decreased by ~0.05 eV compared with the TiO$_2$ (Fig. 4a), and the O 1s BE values of lattice oxygen and surface hydroxyl oxygen decreased by ~0.05 and ~0.13 eV (Fig. 4b), respectively. These results indicate that the calcined residue (CoN$_x$) of CoPy$_4$ molecules are mainly loaded on the primary TiO$_2$ nanoparticles, thus affecting the chemical environment of its surface hydroxyl group [11], and then causing the TiO$_2$ obtaining electrons from the CoN$_x$ clusters.

The high-resolution N 1s spectra (Fig. 4c) indicate that CoPy$_4$ has two BE peaks at 398.48 and 399.00 eV, attributed to the pyridine N atoms outside the CoPy$_4$ molecule and pyrrole N atoms in porphyrin ring [32], respectively. The CoN$_x$/TiO$_2$ shows a greatly changed N 1s XPS spectrum with only one N 1s BE peak at 400.24 eV, which is very close to that of N 1s in the Ni-N single-atom catalysts [27,28]. Nevertheless, the BE value is increased by ~1.76 and ~1.24 eV compared with the pyridine and pyrrole N atoms of CoPy$_4$ molecule, respectively. It demonstrates that the local coordination environments of CoN$_x$ are very different from the CoPy$_4$ molecule because the pyridine and pyrrole N structures in CoPy$_4$ were destroyed after the calcination, while the Co-N$_4$ coordinate covalent bonds can be partially retained on primary TiO$_2$ nanoparticles. Compared with CoPy$_4$, the electron cloud density of N atoms was significantly reduced, indicating that the pyrolysis of CoPy$_4$ molecules entering the Mil-125 micropores leads to the formation of CoN$_x$ clusters, which are close contact with the primary nanoparticles of TiO$_2$ generated by Mil-125.

The high-resolution Co 2p spectrum (Fig. 4d) shows that CoPy$_4$ has two main BE peaks at 781.32 and 796.66 eV, indicating its Co element existing mainly as Co^{2+} species [19]. However, the CoN$_x$/TiO$_2$ exhibits the BE peaks of Co 2p$_{3/2}$/2p$_{1/2}$ at 780.47/795.79 eV, indicating that the electron cloud density of Co^{2+} species in CoN$_x$/TiO$_2$ is higher than that of Co^{2+} species in CoPy$_4$. It indirectly reflects that CoPy$_4$/Mil-125 composite could produce a reducing atmosphere during the calcination,

which allows the Co-N$_4$ subunits in CoPy$_4$ molecule to be partly retained to form CoN$_x$ cluster without being oxidized to CoO$_x$. By considering that the electron cloud densities of Ti and O elements in CoN$_x$/TiO$_2$ decreased compared with TiO$_2$, while that of N element in CoN$_x$/TiO$_2$ increased significantly compared with CoPy$_4$ as mentioned above, it can be inferred that a close contact is formed between CoN$_x$ clusters and TiO$_2$ primary nanoparticles via Ti-O-N-Co bond connection. Compared with the CoN$_x$/TiO$_2$, the BE values of Co 2p in the CoO$_x$/TiO$_2$ increased by ~0.45 eV (Fig. 4d), while that of Ti and lattice O in the CoO$_x$/TiO$_2$ decreased by ~0.09 and ~0.02 eV (Fig. 4a,b), respectively. These results strongly prove that the local chemical environment at Co species in the CoN$_x$/TiO$_2$ is significantly different from that in the CoO$_x$/TiO$_2$.

After 15 min UV-Vis light irradiation, the BE values of Ti 2p of TiO$_2$ shifts negatively by ~0.04 eV, while that of lattice O 1s shifts positively by ~0.03 eV (Fig. 4a,b), both of them are basically negligible. However, the light illumination makes the BE values of Ti 2p and lattice O 1s in the CoN$_x$/TiO$_2$ shifted positively by ~0.07 and ~0.18 eV, respectively. In addition, the BE values of N 1s in the CoN$_x$/TiO$_2$ increased by ~0.08 eV (Fig. 4c), while the BE value of Co 2p shifted negatively by ~0.19 eV after the illumination (Fig. 4d). These results demonstrate that the photogenerated electrons of TiO$_2$ in the CoN$_x$/TiO$_2$ can be rapidly transferred to the Co sites via the coordinated N$_x$ of CoN$_x$ clusters, which then serve as the active sites to receive the photogenerated electrons for catalyzing CO$_2$RR.

The Co K-edge absorption of X-ray absorption near-edge structure (XANES) spectra were measured for further exploring the local coordination environments of the CoN$_x$ clusters. The Co K-edge pre-edge peak position of CoN$_x$/TiO$_2$ is close to that of the CoPy$_4$ and CoO reference, but away from that of the Co foil (Fig. 5a). It indirectly confirms that the calcination of CoPy$_4$/Mil-125 composite would produce a reducing atmosphere, which allows the Co-N$_4$ subunits of CoPy$_4$ molecules to be partly retained without being oxidized to CoO$_x$. Besides, the slightly negative edge-position of the CoN$_x$/TiO$_2$ compared to the CoPy$_4$ implies the increased electron density of Co centers in the CoN$_x$ clusters [19,29]. Nevertheless, the CoO$_x$/TiO$_2$ displays obvious positive edge-position compared with the CoN$_x$/TiO$_2$ and CoO, suggesting the hydrolysates
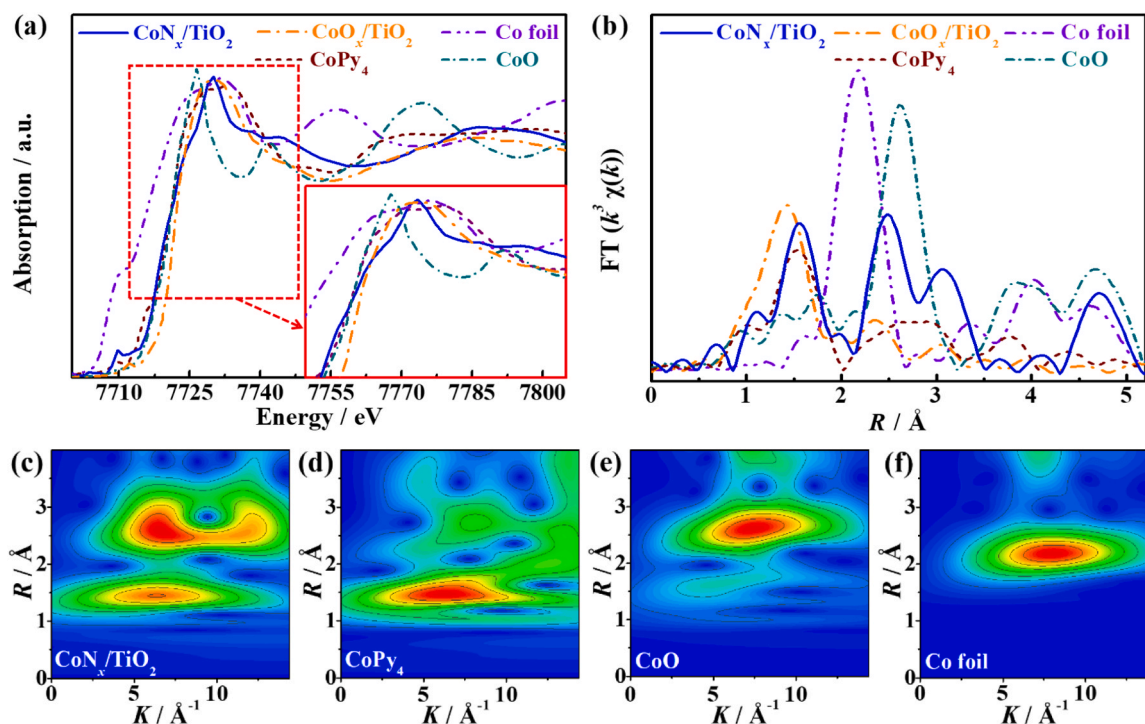

Fig. 5. (a,b) Co K-edge XANES signals (a) and the Fourier transformed radial distribution functions of k^3-weighted $\chi(k)$-function of EXAFS spectra (b) of the CoN$_x$/TiO$_2$, CoO$_x$/TiO$_2$, CoPy$_4$, CoO and Co foil. (c-f) Wavelet transform plots for Co K-edges of the CoN$_x$/TiO$_2$ (c), CoPy$_4$ (d), CoO (e) and Co foil (f).

of $CoCl_2$ adhered on Mil-125 particles would be partly oxidized after the calcination, and thus displaying lower electron density to form CoO_x clusters.

Fourier transformed radial distribution functions (Fig. 5b) of k^3-weighted extended X-ray absorption fine structure (EXAFS) oscillations of Co K-edge (Fig. S7) indicate that the CoN_x/TiO_2 has a clear peak at *ca.* 1.56 Å, ascribable to the Co-N first coordination shell of the CoN_x clusters, which is similar to that of $CoPy_4$ molecule with a clear peaks at 1.54 Å, indicating that the CoN_x may come from the Co-N$_4$ subunits of $CoPy_4$ molecules. Besides, no Co-Co coordination peak at 2.17 Å (for Co-Co bond of the Co foil) and 2.61 Å (for Co-Co bond of the CoO) can be observed from the CoN_x/TiO_2. The wavelet transform plots of the CoN_x/TiO_2 display that their Co-coordinated skeleton pattern (Fig. 5c) is more similar to the $CoPy_4$ (Fig. 5d), but far away from the CoO (Fig. 5e) and Co foil (Fig. 5f), demonstrating the CoN_x clusters have mainly Co-N bonds around the Co centers [19,29]. The EXAFS fitting results (Table S1) show that the slight decreases in the fitting Co-N bond length (R) and coordination number ($N = 3.2$) of the CoN_x clusters compared with the $CoPy_4$ correspond to the above increased electron cloud density on the Co centers of the CoN_x clusters. These results suggest that the CoN_x clusters of CoN_x/TiO_2 are single-atom active sites as confirmed by the above AC-HAADF-STEM images (Fig. 3c,d).

Based on the above spectroscopic characterization results, it can be concluded that $CoPy_4$ molecules in the $CoPy_4$/Mil-125 composite can enter the MOF's micropores, which undergo pyrolysis to form CoN_x clusters containing single-atom sites and Co-N coordination structure under the localized reducing atmosphere due to the calcination of Mil-125. Those CoN_x clusters are uniformly dispersed on the ultrafine primary TiO_2 nanoparticles with close contact *via* Ti-O-N-Co bonds, which

are beneficial for promoting the photogenerated electrons transferring from TiO_2 to CoN_x. However, the hydrolysates of $CoCl_2$ is difficult to enter the micropores of Mil-125, making it prone to generate CoO_x on the TiO_2 aggregated particle surface after the calcination. These structural and physical properties of the CoN_x/TiO_2 will contribute to the effective transfer and separation of photogenerated charge carriers, adsorption and activation of reactants during the photocatalytic process, thereby improving the photoactivity as confirmed below.

3.3. Photocatalytic CO₂RR performance

The control experiments showed that CH_4 and CO were the main CO_2RR products in the present photoreaction system with a 300 W Xe-lamp as light source, and no other reduction products were detected. In addition, no obvious reduction products were detected in the photocatalytic system without photocatalyst, CO_2 gas, or light illumination, indicating that CH_4 and CO were produced by the reduction reactions of reactants (CO_2/H_2O) on photocatalyst. In addition, isotope $^{13}CO_2$ tracing experiment (Fig. S8) determined using gas chromatography-mass spectroscopy (GC-MS) demonstrated that the produced $^{13}CH_4$ and ^{13}CO gases are generated by the $^{13}CO_2$ photoreduction.

Fig. 6a depicts the photocatalytic CO_2RR activity of various samples after 1 h Xe-lamp full spectrum (UV-Vis) light irradiation. The single TiO_2 shows relatively low CO/CH_4 yields of 11.2/2.7 μmol g^{-1} h^{-1}, corresponding an overall photoactivity (total consumed electron number, TCEN) of *ca.* 94.8 μmol g^{-1} h^{-1} calculated using Eq. (1). Those CoN_x/TiO_2 products derived from different $CoPy_4$ addition amounts per 500 mg Mil-125 exhibit much better photoactivity with different CO/CH_4 yields (Fig. 6a,b). Along with the $CoPy_4$ addition amount increased
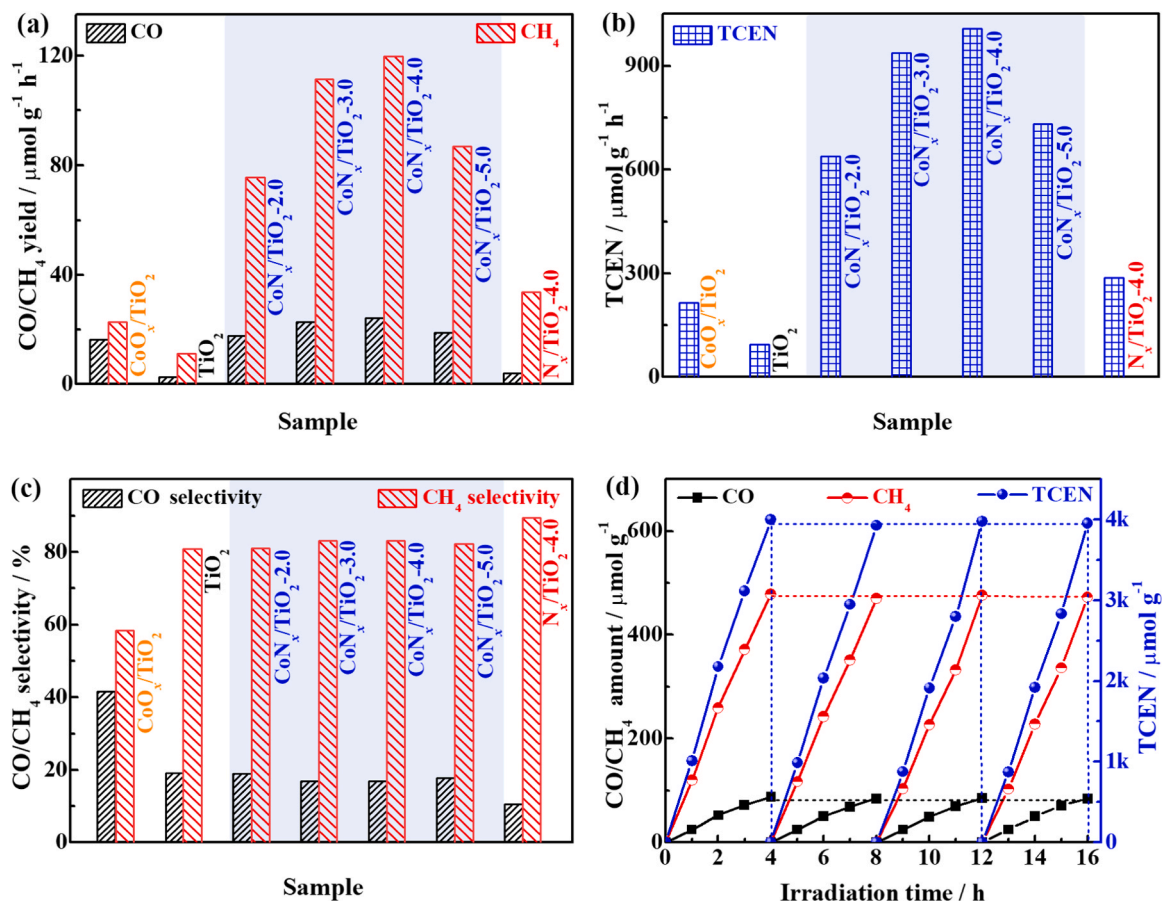

Fig. 6. (a,b) CO/CH₄ yields (a) and the corresponding overall photoactivities (b) of the TiO₂, CoO$_x$/TiO₂, N$_x$/TiO₂ and various CoN$_x$/TiO₂ products under Xe-lamp illumination. (c) CO/CH₄ selectivity (mole percentage) in the CO₂RR systems containing TiO₂, CoO$_x$/TiO₂, N$_x$/TiO₂ and various CoN$_x$/TiO₂ products. (d) Time courses of the CO/CH₄ and the corresponding total photoactivities of the CoN$_x$/TiO₂ with an optimal component ratio.

from 2.0 mg to 4.0 mg, the corresponding products display slightly increased CO yields and more obviously increased CH_4 yields. For example, CO yield slightly increases from 17.8 (CoN_x/TiO_2-2.0) to 24.4 (CoN_x/TiO_2-4.0) $\mu mol\ g^{-1}\ h^{-1}$, while CH_4 yield increases significantly from 75.5 (CoN_x/TiO_2-2.0) to 119.9 (CoN_x/TiO_2-4.0) $\mu mol\ g^{-1}\ h^{-1}$. Once the addition amount is increased to 5.0 mg, the resultant product (CoN_x/TiO_2-5.0) shows decreased CO/CH_4 yields (18.8/86.8 $\mu mol\ g^{-1}$ h^{-1}). Namely, CoN_x/TiO_2-4.0 has the highest CO/CH_4 yields (24.4/ 119.9 $\mu mol\ g^{-1}\ h^{-1}$) with a TCEN of 1007.6 $\mu mol\ g^{-1}\ h^{-1}$, 10.6 and 4.6 times higher than that of the TiO_2 (94.8 $\mu mol\ g^{-1}\ h^{-1}$) and CoO_x/TiO_2 (215.6 $\mu mol\ g^{-1}\ h^{-1}$ with CO/CH_4 yields of 16.2/22.9 $\mu mol\ g^{-1}\ h^{-1}$) (Fig. 6a,b), respectively.

Moreover, those photocatalysts display different CH_4 product selectivity [= (CH_4 yield)/(CO yield + CH_4 yield) $\times$ 100%] (Fig. 6c). Once again, CoN_x/TiO_2-4.0 displays the highest CH_4 selectivity (83.1%) among those CoN_x/TiO_2 products, which is also higher than that of CoO_x/TiO_2 (58.5%) and TiO_2 (80.8%) (Fig. 6c), indicating that the CoN_x clusters in the CoN_x/TiO_2 can effectively improve the CH_4 selectivity compared to the CoO_x/TiO_2. These results imply that the CoN_x/TiO_2 derived from the $CoPy_4$/Mil-125 composite with a weight ratio of 4:500 would has the optimal component ratio for CO_2RR, which was named as CoN_x/TiO_2 for simplicity. By replacing the $CoPy_4$ with metal-free tetra (4-pyridyl)porphyrin (H_2Py_4) with the same weight ratio, the corresponding calcined product (N_x/TiO_2) exhibits much lower photoactivity with CO/CH_4 yields of 4.0/33.8 $\mu mol\ g^{-1}\ h^{-1}$ (Fig. 6a), corresponding to an overall photoactivity (TCEN) of 278.8 $\mu mol\ g^{-1}\ h^{-1}$ (Fig. 6b), 2.9 times higher than that (94.8 $\mu mol\ g^{-1}\ h^{-1}$) of the TiO_2 alone, and slightly higher than that (215.6 $\mu mol\ g^{-1}\ h^{-1}$) of the CoO_x/TiO_2, suggesting that the N_x clusters derived from the pyrolysis of H_2Py_4 may be more beneficial for the adsorption and activation of reactants ($CO_2/$

H_2O) than the CoO_x, thereby improving the photoactivity of TiO_2. The CoN_x/TiO_2 delivers high CO/CH_4 yields (24.4/119.9 $\mu mol\ g^{-1}\ h^{-1}$), CH_4 selectivity (83.1%) and overall photoactivity (1007.6 $\mu mol\ g^{-1}\ h^{-1}$), which is superior to most of the recently reported inorganic-organic hybrid or single-atom photocatalysts for CO_2RR (Table S2) [20,23,32], indicating that it has the potential to actually implement solar-driven CO_2RR for hydrocarbon fuels production.

The cyclic stability of the CoN_x/TiO_2 with an optimal component ratio was further tested under Xe-lamp irradiation for each cycle of 4 h with a total of 12 h photoreaction, and the CO/CH_4 produced amounts and the corresponding total photoactivities for the four photocatalytic cycles are shown in Fig. 6d. The average CO/CH_4 yields in the first run reach 87.2/478.2 $\mu mol\ g^{-1}$, which slightly reduced to 84.5/470.0 μmol g^{-1} in the second run, and remain at 85.27/476.6 and 84.41/473.0 μmol g^{-1} after the third and fourth runs, respectively. Moreover, the average TCEN values (overall photoactivity) for the production of CO/CH_4 only slightly decreases from 1000.0 $\mu mol\ g^{-1}\ h^{-1}$ in the first run to 988.2 $\mu mol\ g^{-1}\ h^{-1}$ in the fourth run, indicating that the CoN_x/TiO_2 as photocatalyst has relatively good stability. The morphology, microstructure (Fig. S9) and XRD pattern (Fig. S10) of the recovered CoN_x/TiO_2 after the 16 h photoreaction are very similar to the original one. Moreover, the binding energy positions of those high-resolution Ti 2p, O 1 s, N 1 s and Co 2p XPS spectra of the recovered CoN_x/TiO_2 have not changed significantly (Fig. S11). These results demonstrate that the present CoN_x/TiO_2 has excellent durability for photocatalytic CO_2RR.

3.4. Energy band structure and photocatalytic mechanism analyses

From the solid-state UV-Vis diffuse reflectance absorption spectra (DRS, Fig. 7a), it can be found that the absorption edge of the single TiO_2
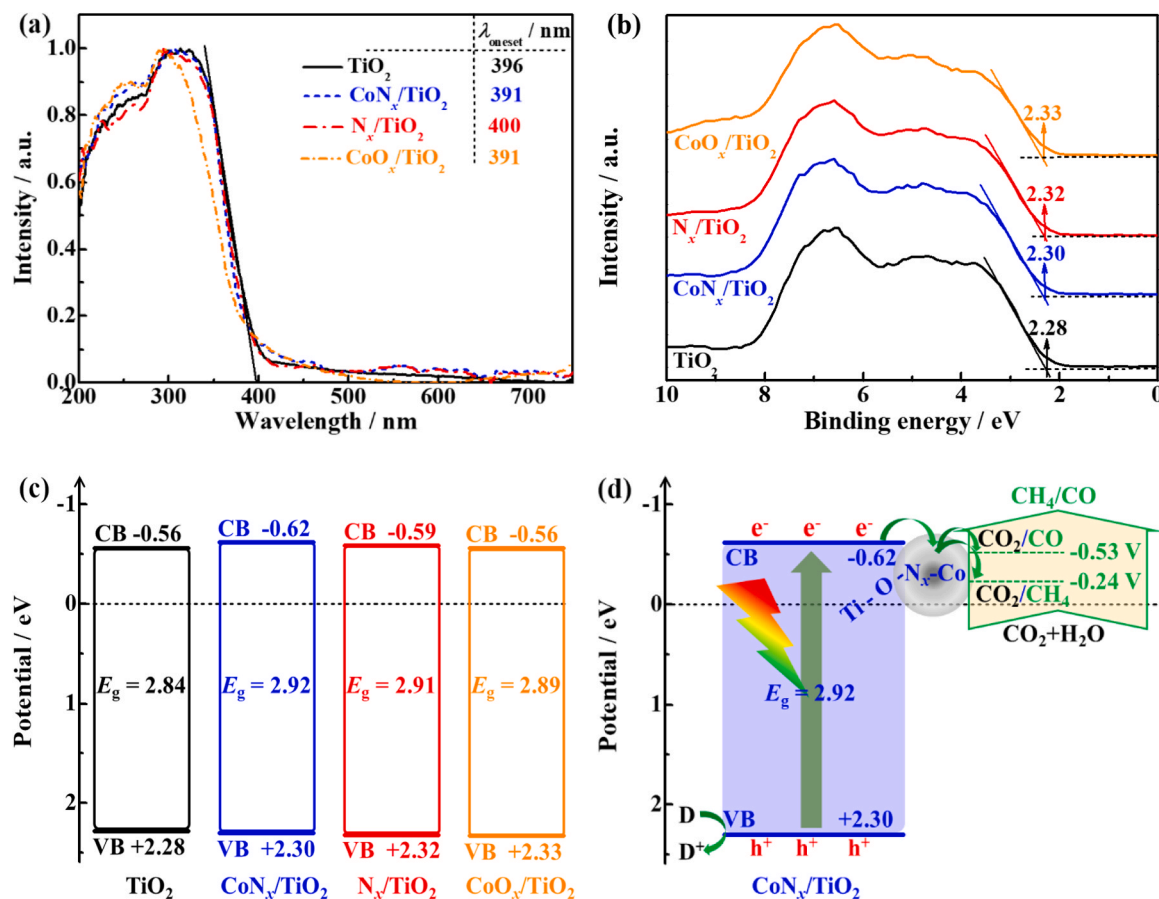

Fig. 7. (a-c) DRS spectra (a), VB XPS spectra (b) and energy band structures (c) of the TiO_2, N_x/TiO_2, CoN_x/TiO_2 and CoO_x/TiO_2. (d) The possible photocatalytic CO_2RR mechanism of the CoN_x/TiO_2.

is ~396 nm, and the CoN_x/TiO_2 show a spectral absorption range similar to the TiO_2. From those Tauc plots $[(\alpha h\nu)^n \sim h\nu$, n = 1/2] derived from the DRS spectra, the energy gap (E_g) of the TiO_2, N_x/TiO_2, CoN_x/TiO_2 and CoO_x/TiO_2 can be estimated as 2.84, 2.91, 2.92 and 2.89 eV (Fig. S12), respectively. That's, those materials have very similar spectral absorption feature, and thus their different photoactivities may be likely attributed to the differences in other aspects such as photogenerated charge separation of TiO_2, adsorption/activation of reactants (CO_2/H_2O) or catalytic ability for CO_2RR.

The valence band (VB) XPS spectra (Fig. 7b) show that the TiO_2, N_x/TiO_2, CoN_x/TiO_2 and CoO_x/TiO_2 have their VB tom (E_{VB}) at 2.28, 2.32, 2.30 and 2.33 eV [11], respectively. Correspondingly, the conduction band (CB) bottom (E_{CB}) of the TiO_2, N_x/TiO_2, CoN_x/TiO_2 and CoO_x/TiO_2 can be calculated as -0.56, -0.59, -0.62 and -0.56 eV according to the equation of $E_{CB} = E_{VB} - E_g$ [9,18], respectively. Therefore, the energy band structures of those materials are summarized in Fig. 7c. As seen, the E_{CB} of TiO_2, N_x/TiO_2, CoN_x/TiO_2 and CoO_x/TiO_2 are negative to the reduction potential of CO_2/CO (-0.53 V *vs.* NHE) and CO_2/CH_4 (-0.24 V *vs.* NHE) (Fig. 7d), indicating that the those materials can achieve CO_2RR to produce CO/CH_4 in thermodynamics [4], which is consistent with the above photocatalytic results, indirectly confirming that the CoN_x and CoO_x clusters in the synthesized composites may mainly serve as cocatalysts to promote the photogenerated charge separation and transfer. However, the CoN_x/TiO_2 delivers greatly improved CO_2RR activity compared with the CoO_x/TiO_2. The possible reason is that the CoN_x clusters as cocatalyst can more effectively promote the rapid transfer/separation of photogenerated charge carriers of TiO_2 and the adsorption/activation of reactants (H_2O/CO_2).

The photocurrent curves (Fig. 8a) exhibit that the CoN_x/TiO_2 has much greater photocurrent response than the TiO_2 and CoO_x/TiO_2, implying that the CoN_x clusters can more effectively promote the separation of photogenerated charge than the CoO_x ones, which is basically similar to their CO_2RR activity (Fig. 6a). The EIS spectra (Fig. 8b) show that those material's electrodes have significant different interfacial charge transfer impedance (R_{ct}) values with the interfacial charge transfer efficiency of $CoN_x/TiO_2 > CoO_x/TiO_2 > TiO_2$, which is consistent with the above results on photocurrent (Fig. 8a) and total photoactivity (Fig. 6a), also indicating that the single-atom Co centers can synergize with the surrounding coordination N_x clusters to act as cocatalyst to more effectively promote the photogenerated charge transfer and separation than the CoO_x clusters, and thereby contributing to the excellent photoactivity for CO_2RR.

The steady photoluminescence (PL, Fig. 8c) and time-resolved fluorescence decay (TRFS, Fig. 8d) spectra further validate the above conjecture. After being excited by 375 nm light, the CoN_x/TiO_2 shows the lowest PL emission intensity, indicating that the CoN_x/TiO_2 has the most efficient charge transfer ability. The TRFS spectra (Fig. 8d) show that the average lifetime of photogenerated electrons in the CoN_x/TiO_2 is 2.02 ns, significantly shorter than the TiO_2 (3.10 ns) and CoO_x/TiO_2 (2.84 ns). This is because the excited state electrons of TiO_2 in the CoN_x/TiO_2 are transferred to the CoN_x clusters, reducing the fluorescence released by the excited state electrons of TiO_2 returning to the ground state, thus reducing the fluorescence lifetime. These results demonstrate that the CoN_x/TiO_2 has the least photogenerated charge recombination, the fastest charge transfer and the smallest charge transfer resistance, thereby promoting the photocatalytic CO_2RR activity.

3.5. Survey on the adsorption and activation of reactants

As mentioned above, liquid N_2 adsorption/desorption experiments

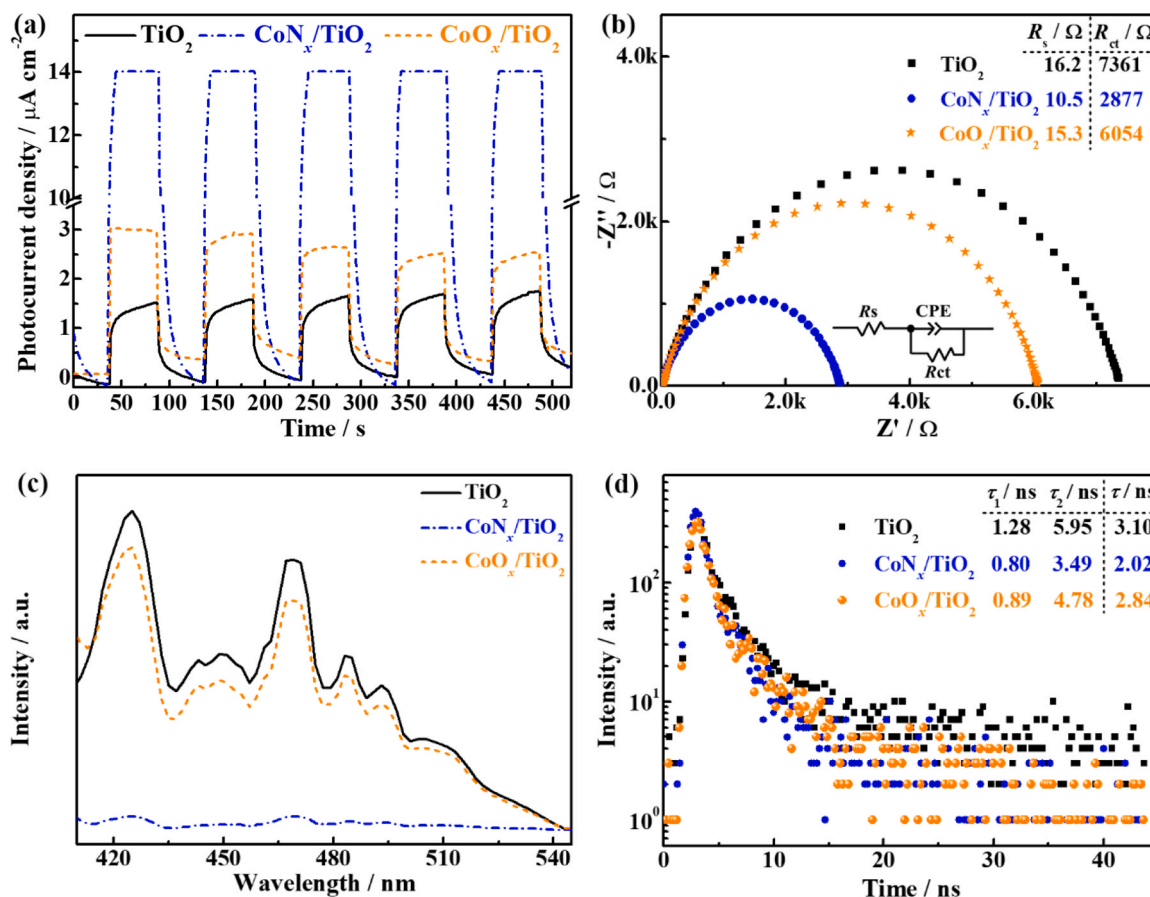**Fig. 8.** Photocurrent (a), EIS (b), photoluminescence (PL) (c, λ_{ex} = 375 nm) spectra and transient fluorescence spectra (TRFS) (d, λ_{ex} = 375 nm, λ_{em} = 400 nm) of the TiO_2, CoN_x/TiO_2 and CoO_x/TiO_2.

demonstrate that both TiO_2 and CoN_x/TiO_2 show type IV isotherm with H3 hysteresis loop and a wide BJH pore size distribution, but the CoN_x/TiO_2 has much larger S_{BET} (75.8 m^2 g^{-1}) and V_{Pore} (0.20 cm^3 g^{-1}) than TiO_2 with a S_{BET} of 30.6 m^2 g^{-1} and a V_{Pore} of ~0.12 cm^3 g^{-1}, while the CoO_x/TiO_2 displays larger S_{BET} (92.4 m^2 g^{-1}) and V_{Pore} (~0.43 cm^3 g^{-1}) than the CoN_x/TiO_2 (Fig. S5 and the corresponding analyses). Generally speaking, a large S_{BET} and V_{Pore} are expected to provide more adsorption and activation sites for CO_2/H_2O, thereby improving the photoactivity. Nevertheless, the above S_{BET} and V_{Pore} are not very consistent with the above CO_2RR activity (Fig. 6a), suggesting that gas adsorption and activation may be one of the main influencing factors of photoactivity in the present gas/solid phase systems. Therefore, temperature programmed desorption-mass spectrometry (TPD-MS) was used to further investigate the influence of CoN_x clusters on the adsorption and activation of reactants (CO_2/H_2O).

From the H_2O-TPD-MS profiles (Fig. 9a), it can be seen that the single TiO_2 exhibits a wide chemical desorption peak at ~225 ℃, while the CoO_x/TiO_2 exhibits a chemical desorption peaks at higher temperature with peaks at ~235 and ~504 ℃, indicating that CoO_x clusters can enhance the adsorption and activation of H_2O. Overall, the CoN_x/TiO_2 shows much higher desorption temperature centered at ~505 ℃ with a narrower temperature range than the TiO_2 and CoO_x/TiO_2. The CO_2-TPD-MS profiles (Fig. 9b) show that the single TiO_2 exhibits a weak CO_2 physical desorption peak at ~116 ℃ and a very wide weak CO_2 chemical desorption peak in a range of 200–800 ℃, while the CoO_x/TiO_2 displays a weak CO_2 physical desorption peak at ~108 ℃ similar to the TiO_2, and a slightly strong chemical desorption peaks centered at ~671 ℃, indicating that the CoO_x clusters can enhance the adsorption and activation of CO_2. Once again, the CoN_x/TiO_2 exhibits CO_2 chemical desorption peaks in a wide temperature range with higher desorption temperatures, indicating that the single-atom Co centers in CoN_x clusters can more effectively improve the adsorption and activation of CO_2 on the CoN_x/TiO_2. Moreover, these TPD-MS results indicate that both H_2O-TPD-MS and CO_2-TPD-MS profiles of the CoN_x/TiO_2 are different from those of the CoO_x/TiO_2 and TiO_2, which reason may be attributed to two aspects: 1) The formation of hydrogen bonds between H_2O and N atoms of CoN_x clusters in the CoN_x/TiO_2, which leads to the CoN_x/TiO_2 showing much higher desorption temperature than the TiO_2 and CoO_x/TiO_2 as shown in Fig. 9a. 2) The electronic configuration and axial coordination ability of the single-atom Co centers in the CoN_x clusters possibly make the CoN_x/TiO_2 having stronger chemical binding ability to CO_2 as shown in Fig. 9b. That's, the CoN_x clusters containing single-atom centers can promote the adsorption and activation of H_2O and CO_2, which is one of the internal reasons why the CoN_x/TiO_2 displays the much higher CO_2RR activity and CH_4 selectivity than the TiO_2 and CoO_x/TiO_2 as shown in Fig. 6a-c.

Based on the above results and discussion, it can be speculated that the introduction of $CoPy_4$ molecules into the Mil-125′s micropores can not only improve the specific surface area and pore volume of the CoN_x/TiO_2, but also its calcined residue can form CoN_x clusters containing single-atom Co sites on the primary TiO_2 nanoparticles with close contacts *via* Ti-O-N-Co bonds, and serve as active sites of TiO_2 to enrich the photogenerated electrons and activate the reactants (CO_2/H_2O) under light illumination, thus contributing to the significantly improved photocatalytic CO_2RR activity through the mechanism shown in Fig. 7d.

4. Conclusions

In summary, a novel single-atom CoN_x clusters-decorated TiO_2 (CoN_x/TiO_2) was synthesized *in situ* by calcining a composite derived from immersing Mil-125 into $CoPy_4$ solution. Spectroscopic and electron microscopic analysis results demonstrate that the $CoPy_4$ molecules are easier to enter the micropores of the Mil-125 than the hydrolysates of $CoCl_2$, which helps to pyrolyze the $CoPy_4$ molecules into highly dispersed CoN_x clusters with single-atom catalytic sites and to form strong interaction with the primary nanoparticles of TiO_2 *quasi*-nano-cube-like aggregated particles derived from the Mil-125. These factors of the CoN_x/TiO_2 enable efficient photogenerated charge separation, strong chemical adsorption to reactants and high atom utilization, thereby the resultant CoN_x/TiO_2 delivers an excellent CO_2RR activity with CO/CH_4 yields of 24.4/119.9 μmol g^{-1} h^{-1} and CH_4 selectivity of > 80%, corresponding an overall photoactivity of 1007.6 μmol g^{-1} h^{-1}, which is 10.6 and 4.7 times higher than the single TiO_2 and CoO_x/TiO_2, respectively. The present work provides a new strategy for constructing high-efficient TiO_2-based photocatalysts with highly dispersed single-atom catalytic sites (CoN_x), which exhibits significantly better photocatalytic CO_2RR activity than the traditional CoO_x cocatalysts.

CRediT authorship contribution statement

Peng Zeng: Conceptualization, Methodology, Project administration, Writing - original draft. **Haoran Liu**: Investigation, Methodology, Validation, Visualization. **Huaiyang Jia**: Investigation, Data curation. **Jiayi Cai**: Investigation, Visualization. **Xueer Deng**: Investigation, Validation. **Tianyou Peng**: Conceptualization, Project administration, Supervision, Writing - review & editing. All authors have agreed to the signature to the author list.

Declaration of Competing Interest

The authors declare that they have no known competing financial interests or personal relationships that could have appeared to influence the work reported in this paper.
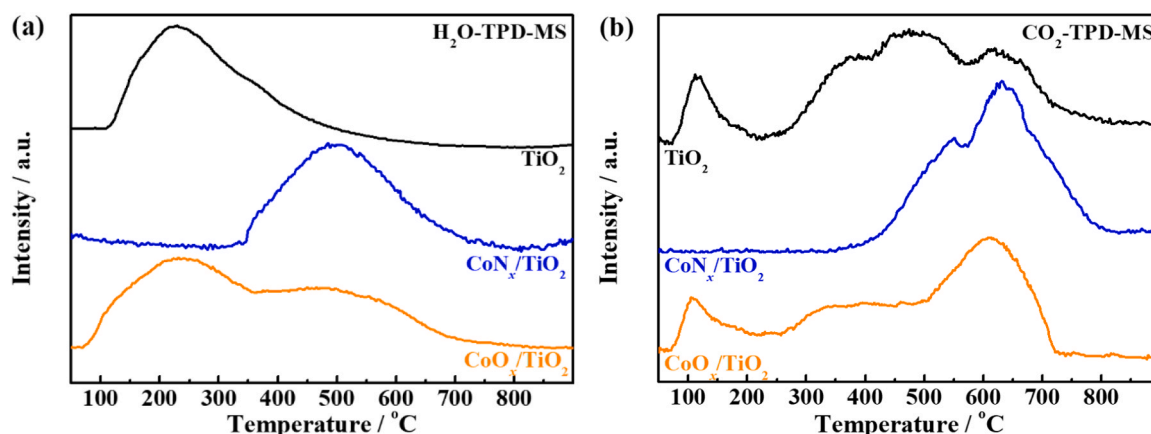

Fig. 9. H_2O-TPD-MS (a) and CO_2-TPD-MS (b) profiles on the TiO_2, CoN_x/TiO_2 and CoO_x/TiO_2.

Data availability

Data will be made available on request.

Appendix A. Supporting information

Supplementary data associated with this article can be found in the online version at doi:10.1016/j.apcatb.2023.123268.

References

[1] D. Kim, K.K. Sakimoto, D. Hong, P. Yang, Artificial photosynthesis for sustainable fuel and chemical production, Angew. Chem. Int. Ed. 54 (2015) 3259–3266.
[2] W.A. Thompson, S.F. Eva, M.M. Maroto-Valer, Review and analysis of CO_2 photoreduction kinetics, ACS Sustain. Chem. Eng. 8 (2020) 4677–4692.
[3] J.J. Yuan, S.T. Chen, Y.Y. Zhang, R.J. Li, J. Zhang, T.Y. Peng, Structural regulation of coupled phthalocyanine-porphyrin covalent organic frameworks to highly active and selective electrocatalytic CO_2 reduction, Adv. Mater. 34 (2022) 2203139.
[4] K. Li, B.S. Peng, T.Y. Peng, Recent advances in heterogeneous photocatalytic CO_2 conversion to solar fuels, ACS Catal. 6 (2016) 7485–7527.
[5] Q. Guo, C. Zhou, Z. Ma, X. Yang, Fundamentals of TiO_2 photocatalysis: Concepts, mechanisms, and challenges, Adv. Mater. 31 (2019) 1901997.
[6] F. Akira, N.R. Tata, A.T. Donald, Titanium dioxide photocatalysis, J. Photochem. Photobiol. C. 1 (2000) 1–21.
[7] H.W. Guo, S.P. Wan, Y.N. Wang, W.H. Ma, Q. Zhong, J. Ding, Enhanced photocatalytic CO_2 reduction over direct Z-scheme $NiTiO_3$/g-C_3N_4 nanocomposite promoted by efficient interfacial charge transfer, Chem. Eng. J. 412 (2021), 128646.
[8] Z. Jiang, X.H. Xu, Y.H. Ma, H.S. Cho, D. Ding, C. Wang, J. Wu, P. Oleynikov, M. Jia, J. Cheng, Y. Zhou, O. Terasaki, T.Y. Peng, L. Zan, H.X. Deng, Filling metal-organic framework mesopores with TiO_2 for CO_2 photoreduction, Nature 586 (2020) 549–554.
[9] C. Chen, J.P. Jin, S.T. Chen, T.X. Wang, J.R. Xiao, T.Y. Peng, In-situ growth of ultrafine ZnO on g-C_3N_4 layer for highly active and selective CO_2 photoreduction to CH_4 under visible light, Mater. Res. Bull. 137 (2021), 111177.
[10] P. Zhou, J.G. Yu, M. Jaroniec, All-solid-state Z-scheme photocatalytic systems, Adv. Mater. 26 (2014) 4920–4935.
[11] J.R. Xiao, C. Chen, S.T. Chen, H.R. Liu, T.Y. Peng, Insight into the significantly enhanced photocatalytic CO_2 reduction performance of Pt/MnO dual cocatalysts on sea-urchin-like anatase TiO_2 microspheres, Chem. Eng. J. 425 (2021), 131627.
[12] G.H. Li, Y.Y. Sun, Q.M. Zhang, Z. Gao, W. Sun, X.X. Zhou, Ag quantum dots modified hierarchically porous and defective TiO_2 nanoparticles for improved photocatalytic CO_2 reduction, Chem. Eng. J. 410 (2021), 128397.
[13] Y.Z. Zhang, S. Tang, W.D. Zhang, Y.X. Yu, Noble metal-free photocatalysts consisting of graphitic carbon nitride, nickel complex, and nickel oxide nanoparticles for efficient hydrogen generation, ACS Appl. Mater. Interfaces 11 (2019) 14986–14996.
[14] X.J. Guan, S.S. Mao, S.H. Shen, Recent progress on photocatalytic CO_2 reduction with earth-abundant single-atom reactive sites, ChemNanoMat 7 (2021) 873–880.
[15] C. Gao, J. Low, R. Long, T. Kong, J. Zhu, Y. Xiong, Heterogeneous single-atom photocatalysts: Fundamentals and applications, Chem. Rev. 120 (2020) 12175–12216.
[16] X. Ge, P. Zhou, Q. Zhang, Z. Xia, S. Chen, P. Gao, Z. Zhang, L. Gu, S. Guo, Palladium single atoms on TiO_2 as a photocatalytic sensing platform for analyzing the organophosphorus pesticide chlorpyrifos, Angew. Chem. Int. Ed. 59 (2020) 232–236.
[17] T.X. Wang, L.L. Guo, Z. Jiang, S.T. Chen, S.R. Xu, Y.X. Zhang, J. Zhang, R.J. Li, T. Y. Peng, Ru-pincer complex-bridged Cu-porphyrin polymer for robust (photo) electrocatalytic H_2 evolution via single-atom active sites, Adv. Funct. Mater. 31 (2021) 2107290.
[18] J.M. Wang, L. Xu, T.X. Wang, R.J. Li, Y.X. Zhang, J. Zhang, T.Y. Peng, Porphyrin conjugated polymer grafted onto $BiVO_4$ nanosheets for efficient Z-scheme overall water splitting via cascade charge transfer and single-atom catalytic sites, Adv. Energy Mater. 11 (2021) 2003575.
[19] S.T. Chen, P.T. Kong, H. Niu, H.R. Liu, X.T. Wang, J. Zhang, R.J. Li, Y.Z. Guo, T. Y. Peng, Co-porphyrin/Ru-pincer complex coupled polymer with Z-scheme molecular junctions and dual single-atom sites for visible light-responsive CO_2 reduction, Chem. Eng. J. 43 (2022), 133357.
[20] Z.Y. Jiang, W. Sun, W.K. Miao, Z.M. Yuan, G.H. Yang, F.G. Kong, T.J. Yan, J. C. Chen, B.B. Huang, C.H. An, G.A. Ozin, Living atomically dispersed Cu ultrathin TiO_2 nanosheet CO_2 reduction photocatalyst, Adv. Sci. 6 (2019) 1900289.
[21] H.X. Gao, K. Liu, T. Luo, Y. Chen, J.H. Hu, J.W. Fu, M. Liu, CO_2 reduction reaction pathways on single-atom Co sites: Impacts of local coordination environment, Chin. J. Catal. 43 (2022) 832–838.
[22] S.P. Ding, M.J. Hülsey, J. Pérez-Ramírez, N. Yan, Transforming energy with single-atom catalysts, Joule 3 (2019) 2897–2929.
[23] Y. Yu, X. Dong, P. Chen, Q. Geng, H. Wang, J. Li, Y. Zhou, F. Dong, Synergistic effect of Cu single atoms and Au-Cu alloy nanoparticles on TiO_2 for efficient CO_2 photoreduction, ACS Nano 15 (2021) 14453–14464.
[24] Y. Zhou, M.X. Xie, Y. Song, D.K. Yan, Z.L. Wang, S. Zhang, C. Deng, Edge-enriched Ni-N_4 atomic sites embedded enoki-mushroom-like carbon nanotubes assembling hollow fibers for CO_2 conversion and flexible Zn-air battery, Energy Storage Mater. 47 (2022) 235–248.
[25] X. Yang, J. Cheng, X.X. Xuan, N. Liu, J.Z. Liu, Boosting defective carbon by anchoring well-defined atomically dispersed Ni-N_4 sites for electrocatalytic CO_2 reduction, ACS Sustain. Chem. Eng. 8 (2020) 10536–10543.
[26] S. Paul, Y.L. Kao, L.M. Ni, R. Ehnert, H.G. Iris, V.D.K. Roel, R.W. Stark, J. Wolfram, U.I. Kramm, P. Bogdanoff, Influence of the Metal Center in M–N–C catalysts on the CO_2 reduction reaction on gas diffusion electrodes, ACS Catal. 11 (2021) 5850–5864.
[27] G.C. Lei, Y.W. Tong, L.J. Shen, Y. Zheng, S.J. Liang, W. Lin, F.J. Liu, Y.N. Cao, Y. H. Xiao, L.L. Jiang, Highly poison-resistant single-atom Co-N_4 active sites with superior operational stability over 460h for H_2S catalytic oxidation, Small 17 (2021) 2104939.
[28] L.M. Ning, S.Y. Liao, H. Li, R.Y. Tong, C.Q. Dong, M.T. Zhang, W. Gu, X. Liu, Carbon-based materials with tunable morphology confined Ni(0) and Ni-N_x active sites: Highly efficient selective hydrogenation catalysts, Carbon 154 (2019) 48–57.
[29] J.M. Wang, L. Xu, T.X. Wang, S.T. Chen, Z. Jiang, R.J. Li, Y.X. Zhang, T.Y. Peng, Porphyrin conjugated polymer with periodic type II-like heterojunctions and single-atom catalytic sites for broadband-responsive hydrogen evolution, Adv. Funct. Mater. 31 (2021) 2009819.
[30] Y.Y. Zhang, S.T. Chen, Y.X. Zhang, R.J. Li, B. Zhao, T.Y. Peng, Hydrogen-bond regulation of microenvironment of Ni(II)-porphyrin bifunctional electrocatalysts for efficient overall water splitting, Adv. Mater. 35 (2023) 2210727.
[31] Y. Zheng, J.M. Wang, J. Zhang, T.Y. Peng, R.J. Li, Syntheses of asymmetric zinc porphyrins bearing different pseudo-pyridine substituents and their photosensitization for visible-light-driven H_2 production activity, Dalton Trans. 46 (2017) 8219–8228.
[32] H.R. Liu, S.T. Chen, Y.Y. Zhang, R.J. Li, J. Zhang, T.Y. Peng, An effective Z-scheme hybrid photocatalyst based on zinc porphyrin derivative and anatase titanium dioxide microsphere for carbon dioxide reduction, Mater. Today Sustain. 19 (2022), 100164.
[33] Y. Zhang, J. Zhao, H. Wang, B. Xiao, W. Zhang, X. Zhao, T. Lv, M. Thangamuthu, J. Zhang, Y. Guo, J. Ma, L. Lin, J. Tang, R. Huang, Q. Liu, Single-atom Cu anchored catalysts for photocatalytic renewable H_2 production with a quantum efficiency of 56%, Nat. Commun. 13 (2022) 58.
[34] J. Jin, P. Li, D.H. Chun, B.J. Jin, K. Zhang, J.H. Park, Defect dominated hierarchical Ti-metal-organic frameworks via a linker competitive coordination strategy for toluene removal, Adv. Funct. Mater. 31 (2021) 2102511.
[35] M. Dan-Hardi, C. Serre, T. Frot, L. Rozes, C. Maurin, C. Sanchez, G. Férey, A new photoactive crystalline highly porous titanium(IV) dicarboxylate, J. Am. Chem. Soc. 131 (2009) 10857–10859.
[36] B. Ravel, M. Newville, Thena, artemis, hephaestus: Data analysis for X-ray absorption spectroscopy using IFEFFIT, J. Synchrotron Radiat. 12 (2005) 537–541.
[37] J.P. Zhao, Q. Peng, Z.J. Wang, W. Xu, H.Y. Xiao, Q. Wu, H.L. Sun, F. Ma, J.Y. Zhao, C.J. Sun, J.Z. Zhao, J.F. Li, Proton mediated spin state transition of cobalt heme analogs, Nat. Commun. 10 (2019) 2303.
[38] H. Funke, A.C. Scheinost, M. Chukalina, Wavelet analysis of extended X-ray absorption fine structure data, Phys. Rev. B 71 (2005), 094110.